LOW MASS STARS : NUCLEOSYNTHESIS

- FIRST (and SECOND) DREDGE-UP reveal n-s achieved outside core of M-S star

- He-CORE FLASH **?**

- THIRD DREDGE-UP
  - → **FRESH n-s PRODUCTS INTO ENVELOPE**
    - He-burning - ^{12}C, ^{19}F, ...
    - s-process (main)
  - → ISM via $\dot{m}$ on AGB and at end of AGB (planetary neb.)

- HOT BOTTOM CONVECTIVE ENVELOPE IN INTERMEDIATE-MASS AGBs
  - → $^{12}C \rightarrow ^{14}N$; $^{3}He \rightarrow ^{7}Li$
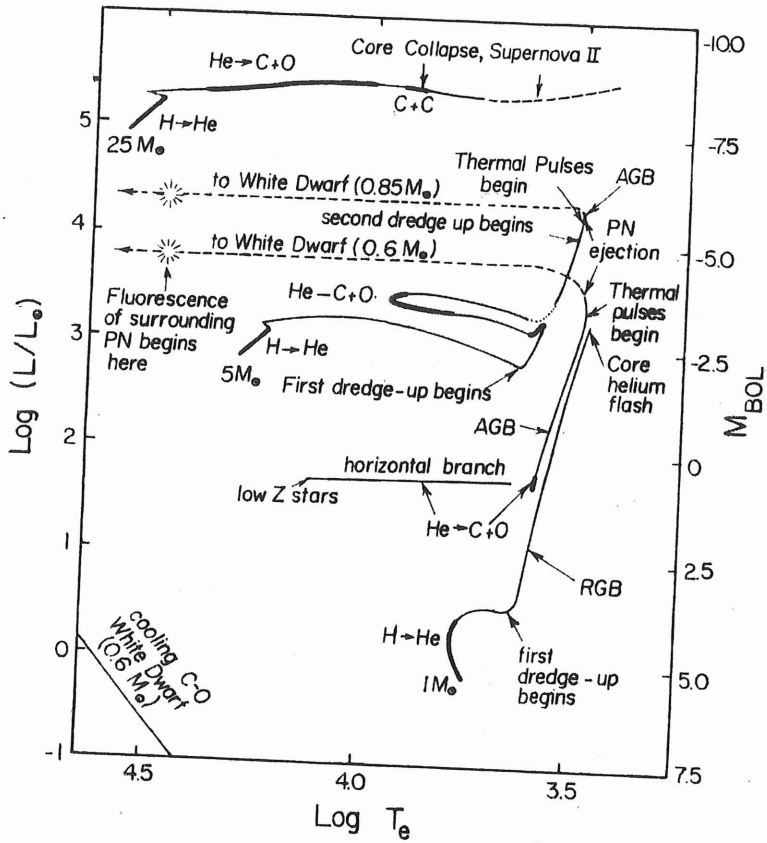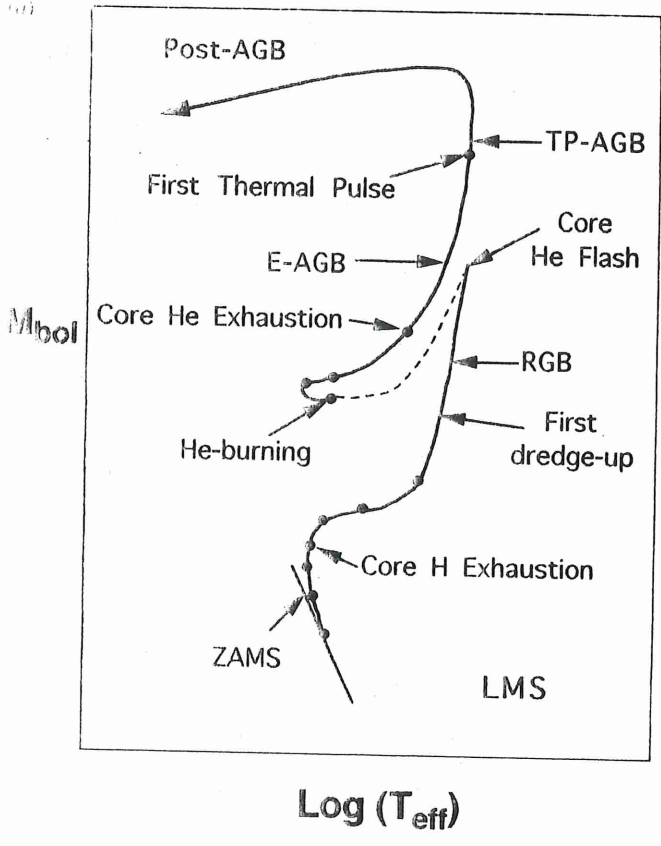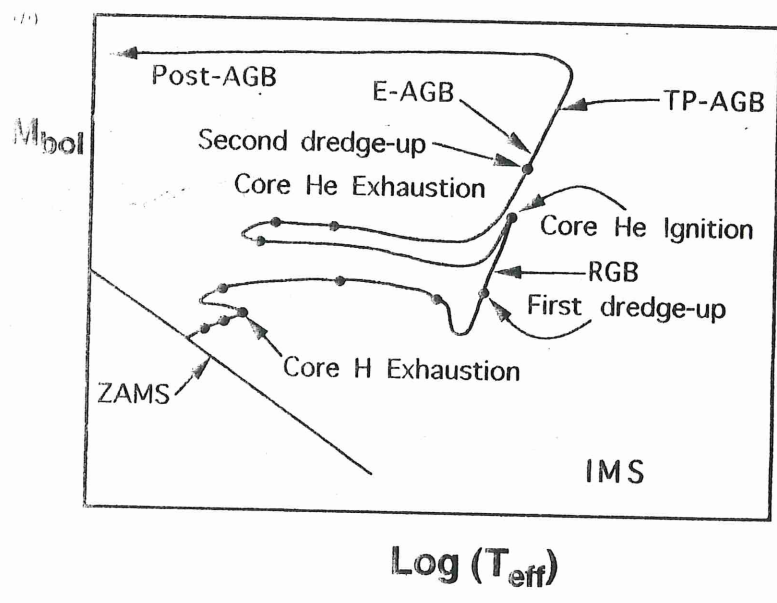 - → ISM as above

EXTRA-MIXING ?

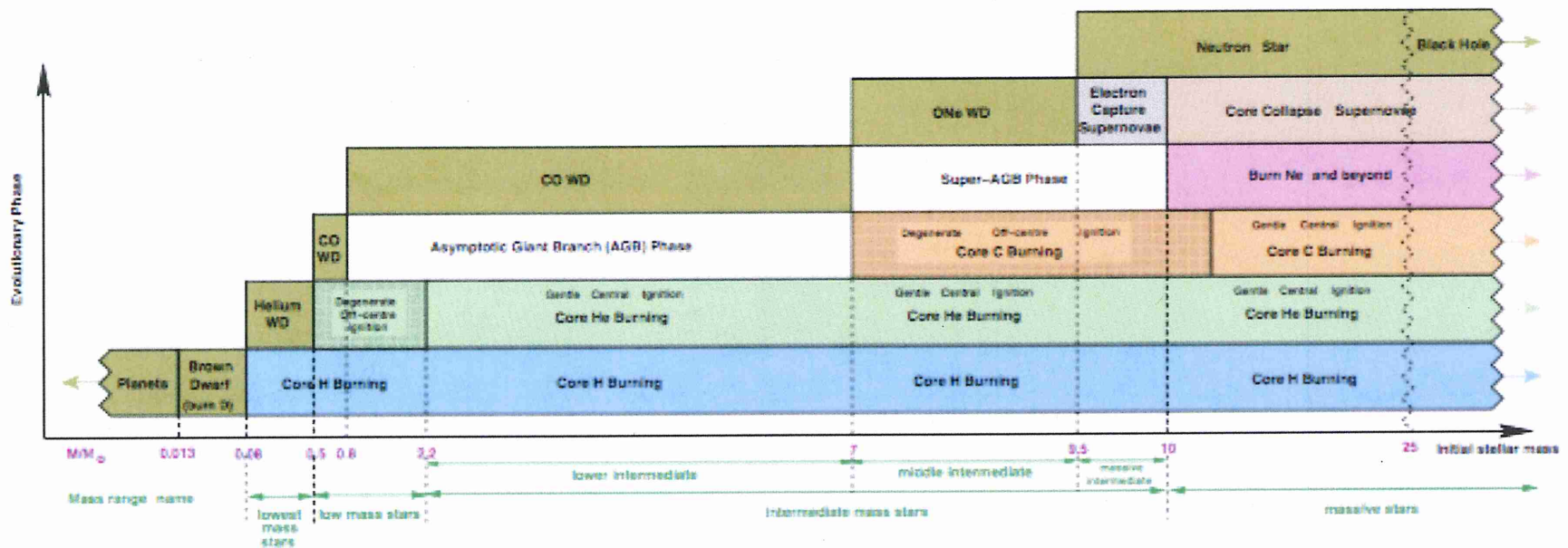**Fig. 5.15.** Evolutionary tracks of stars with mass 1, 5 and 25 $M_\odot$ in the HR diagram. Adapted from Iben (1985, 1991).

Post-AGB

TP-AGB

First Thermal Pulse

Core He Flash

E-AGB

Core He Exhaustion

M_{bol}

RGB

He-burning

First dredge-up

Core H Exhaustion

ZAMS

LMS

Log (T_{eff})

LOW MASS

Post-AGB

E-AGB

TP-AGB

M_{bol}

Second dredge-up

Core He Exhaustion

Core He Ignition

RGB
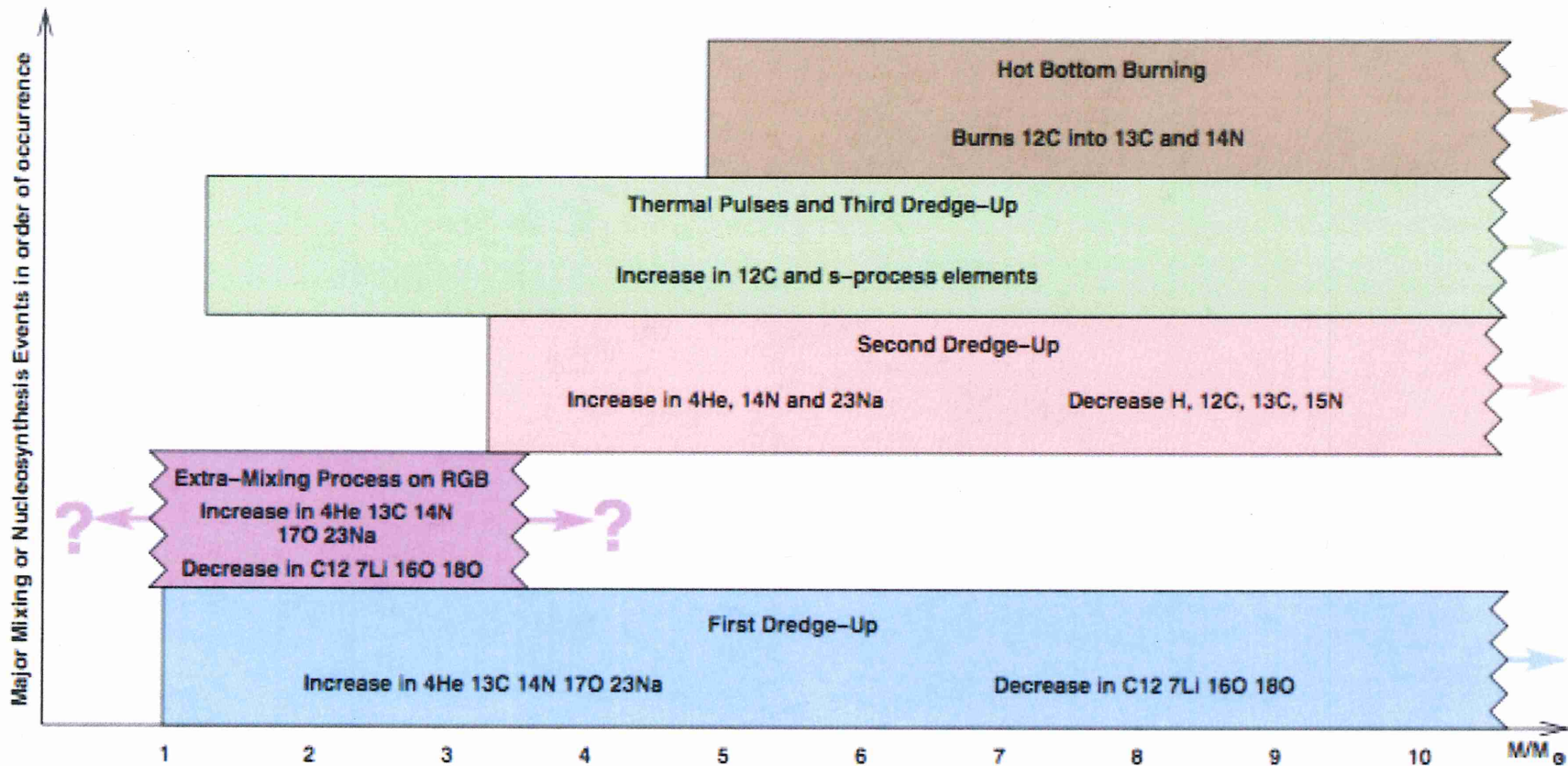
First dredge-up

ZAMS

Core H Exhaustion

IMS

Log (T_{eff})

INTERMEDIATE MASS

Figure 1. Schematic showing how stellar mass determines the main nuclear burning phases at solar metallicity, as well as the fate of the final remnant. This defines the different mass intervals we will deal with in this paper. Note that the borders are often not well determined theoretically, depending on details such as mass loss and the implementation of mixing, for example. This is particularly true for the borders around the region of the electron-capture supernovae. Likewise, all numbers are rough estimates, and depend on composition in addition to details of the modelling process.

Figure 4. A schematic diagram showing the mass dependence of the different dredge-up, mixing, and nucleosynthesis events. The species most affected are also indicated. The lower mass limits for the onset of the SDU, third dredge up, and HBB depend on metallicity and we show approximate values for $Z = 0.02$. Note that the 'extra-mixing' band has a very uncertain upper mass-limit, because the mechanism of the mixing is at present unknown.

FIRST DREDGE-UP

SIGNATURES

$^{12}C/^{13}C \downarrow$ $^{14}N \uparrow$ $(^{12}C + ^{13}C + ^{14}N = \text{constant})$

$^{18}O \downarrow$ $^{17}O \uparrow$ as $f(m)$ $^{16}O \sim$ no change

$^{15}N \downarrow$ Na $\uparrow$ Li $\downarrow$

ISSUES

$^{12}C/^{13}C$ often lower than predicted

high Li in rare cases

$^{3}He(\alpha, \gamma)^{7}Be(e^{-}, \nu)^{7}Li;$ { RGB bump
He-core flash
planets?
x?

SUPPLY
FINITE

$^{17}O, ^{18}O$ obs.?

a)

He-CORE

ZONES PARTIALLY CN PROCESSED

CONVECTIVE ENVELOPE

H-BURNING SHELL (ACTIVE)

LIMIT OF FIRST DREDGE-UP

b)

C-O-CORE

He, N

CONVECTIVE ENVELOPE

He-BURNING SHELL (ACTIVE)

LIMIT OF SECOND DREDGE-UP

H-BURNING SHELL (INACTIVE)
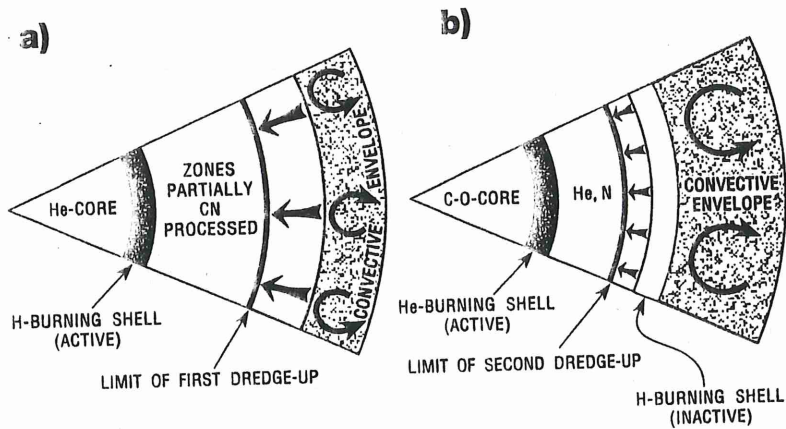
Figure 3 *a*. Sketch of the internal structure of a star at the moment of first dredge-up. The energy is produced by the H-burning shell above the He core. The first dredge-up extends downward to incorporate regions where partial CN processing occurred during the main sequence phase and are thus incorporated into the convective envelope (see Figure 2). *b*. Second dredge-up for intermediate mass stars. Here the energy is produced by the He-burning shell during the time when H burning is extinguished in the H shell. Convection penetrates from the envelope to below the former position of the H shell and hence mixes with the envelope products of H burning.
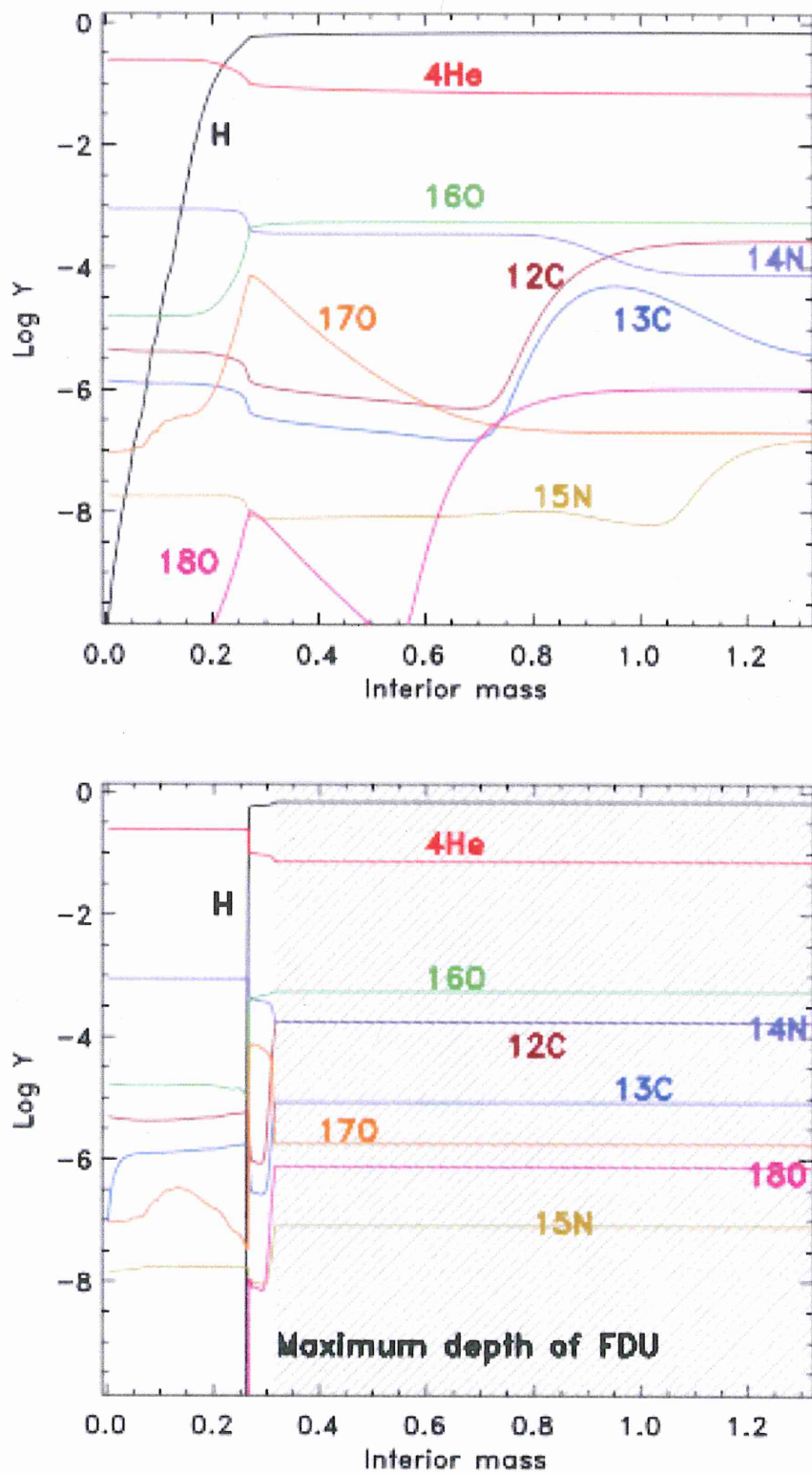
Figure 5. Composition profiles from the $2\,M_\odot$, $Z = 0.02$ model. The top panel illustrates the interior composition after the main sequence and before the FDU takes place, showing mostly CNO isotopes. The lower panel shows the composition at the deepest extent of the FDU ($0.31\,M_\odot$), where the shaded region is the convective envelope. Surface abundance changes after the FDU include: a reduction in the C/O ratio from 0.50 to 0.33, in the $^{12}C/^{13}C$ ratio from 86.5 to 20.5, an increase in the isotopic ratio of $^{14}N/^{15}N$ from 472 to 2 188, a decrease in $^{16}O/^{17}O$ from 2 765 to 266, and an increase in $^{16}O/^{18}O$ from 524 to 740. Elemental abundances also change: [C/Fe] decreases by about 0.20, [N/Fe] increases by about 0.4, and [Na/Fe] increases by about 0.1. The helium abundance increases by $\Delta Y \approx 0.012$.
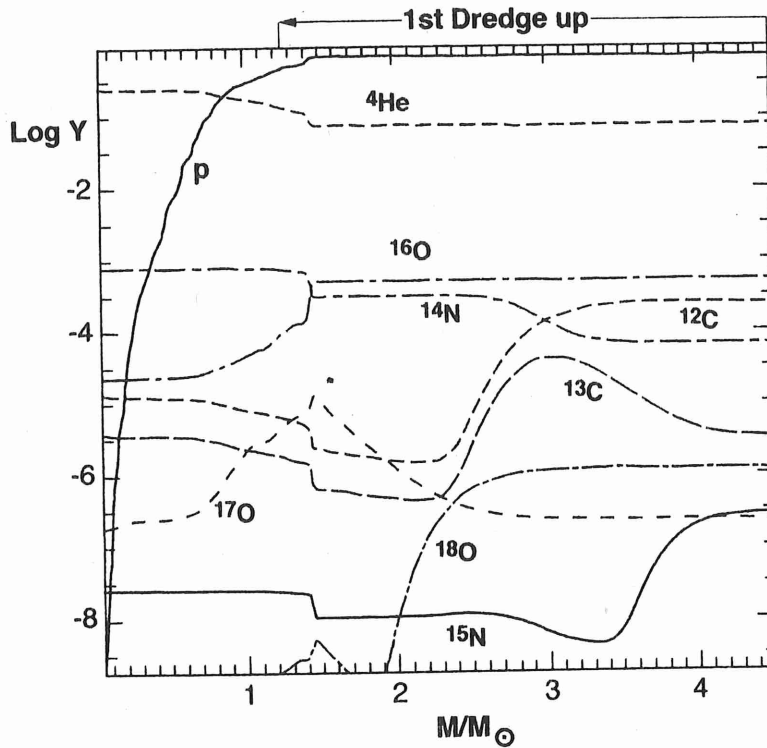
Figure 2 Distribution of the abundances of light nuclei in the inner regions of a 5-$M_\odot$ star with $Z = Z_\odot$ after core hydrogen burning. The region subsequently mixed by the first dredge-up is indicated by the *arrow*. Before first dredge-up, the original composition is unchanged down to $\sim 4.0\ M_\odot$; below that region there are increases in ^{13}C and ^{14}N and sharp decreases in ^{12}C and ^{15}N. After first dredge-up, the envelope composition is then changed to the average value mixed to the depth indicated.

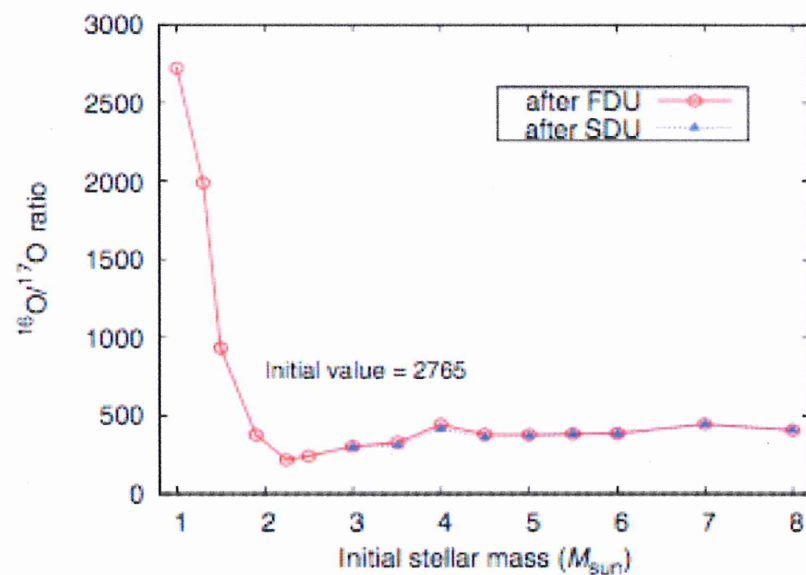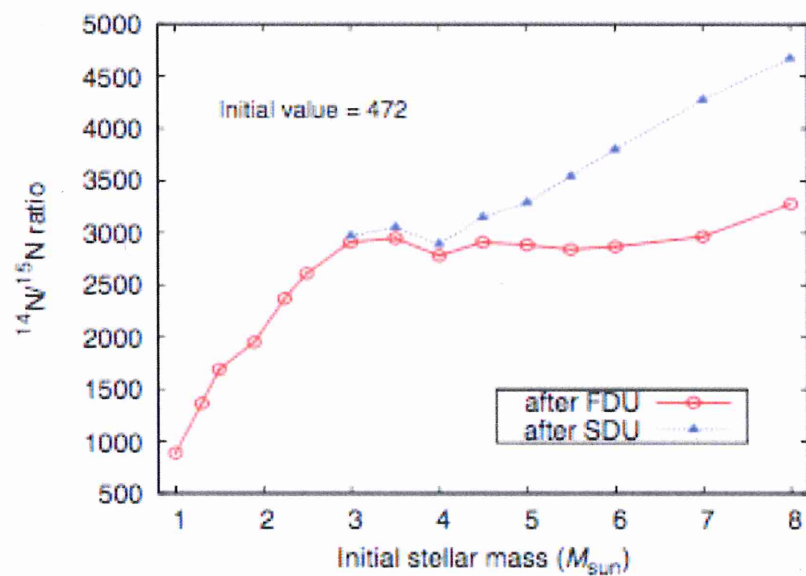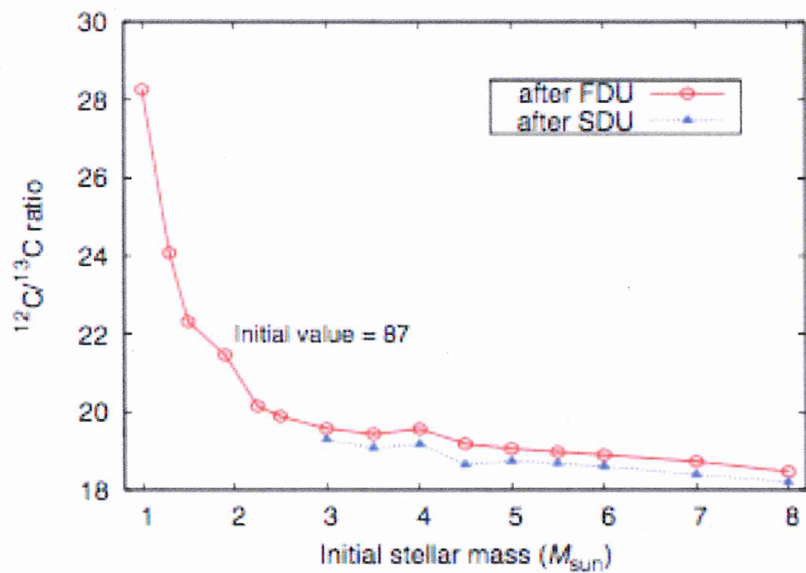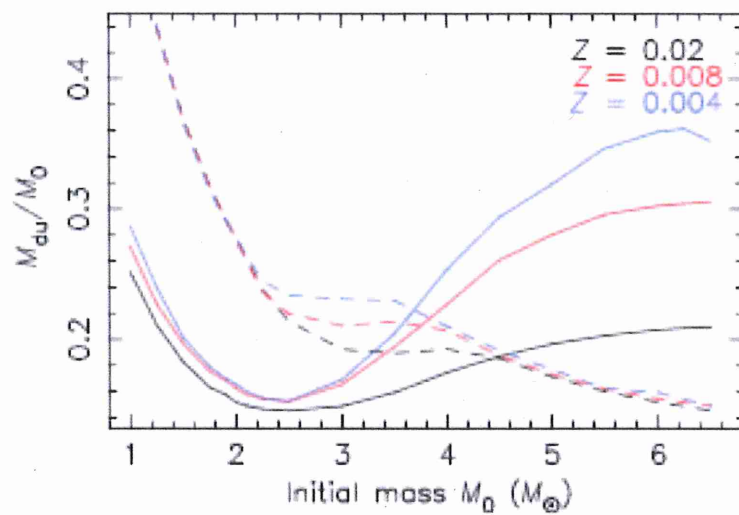**Figure 6.** Surface abundance predictions from $Z = 0.02$ models showing the ratio (by number) of $^{12}C/^{13}C$, $^{14}N/^{15}N$, and $^{16}O/^{17}O$ after the first dredge-up (red solid line) and second dredge-up (blue dotted line).

Figure 7. Innermost mass layer reached by the convective envelope during the first dredge-up (solid lines) and second dredge-up (dashed lines) as a function of the initial stellar mass and metallicity. The mass co-ordinate on the y-axis is given as a fraction of the total stellar mass (M_{du}/M_0)—from Karakas (2003).
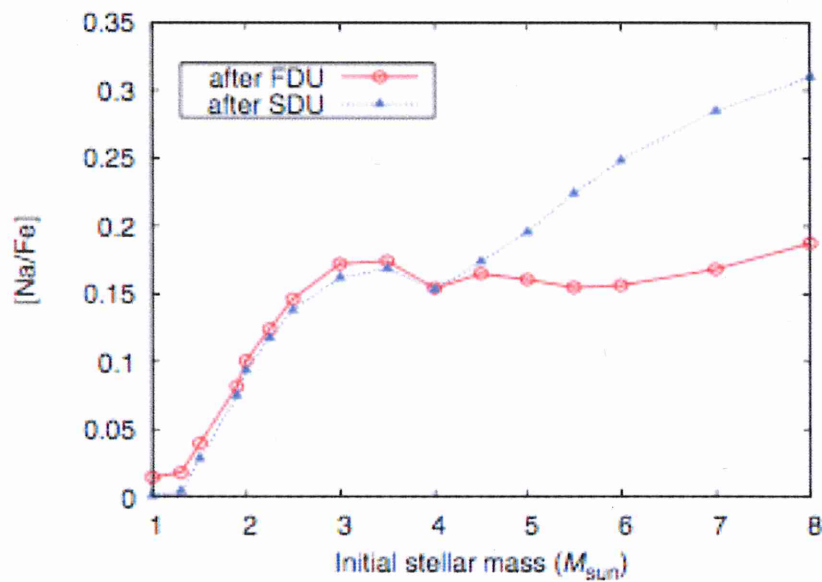
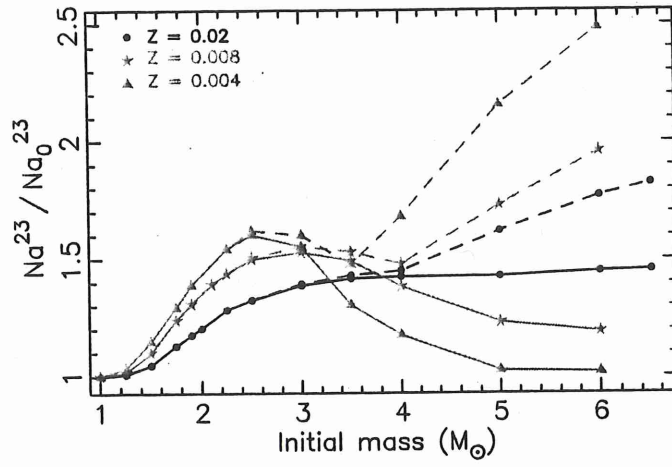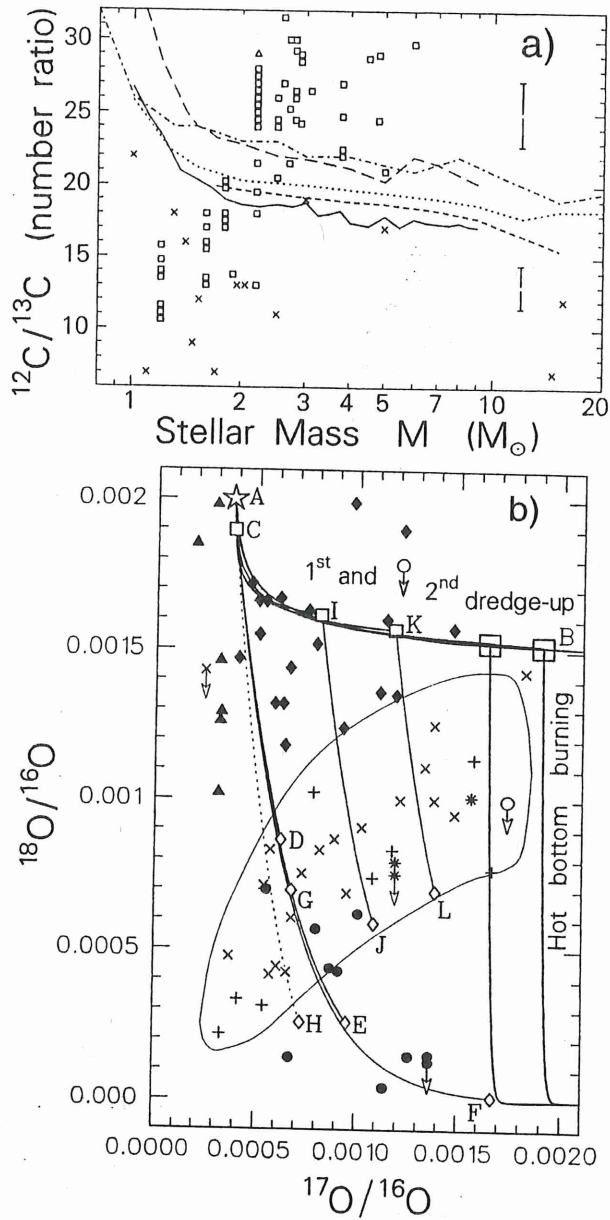**Figure 8.** Predicted [Na/Fe] after the FDU and SDU for the $Z = 0.02$ models.

Fig. 9. The fractional changes to the surface ^{23}Na abundances after the FDU (solid lines) and SDU (dashed lines)

Figure 4 *a*. Comparison of the $^{12}C/^{13}C$ ratios observed in red giant stars with model predictions of first dredge-up, as a function of stellar mass. Note that stars with $M_\odot \leq 2\,M_\odot$ have $^{12}C/^{13}C$ far (10-fold) below the five theoretical curves shown. Stars above this mass have $^{12}C/^{13}C$ typically within ~20% of the theoretical curves shown. *b*. Comparison between observations on oxygen in Al_2O_3 grains formed as circumstellar condensates (*blackened symbols*) and stellar observations (+). Note that the stellar observations have large errors (not shown). The trajectory A–B corresponds to first and second dredge-up for standard stellar models for $Z = Z_\odot$. Trajectories A, D, J, L, and F correspond to cool-bottom-processing conveyor belt calculations (after Wasserburg et al 1995) and data sources cited therein, particularly Nittler et al (1994).
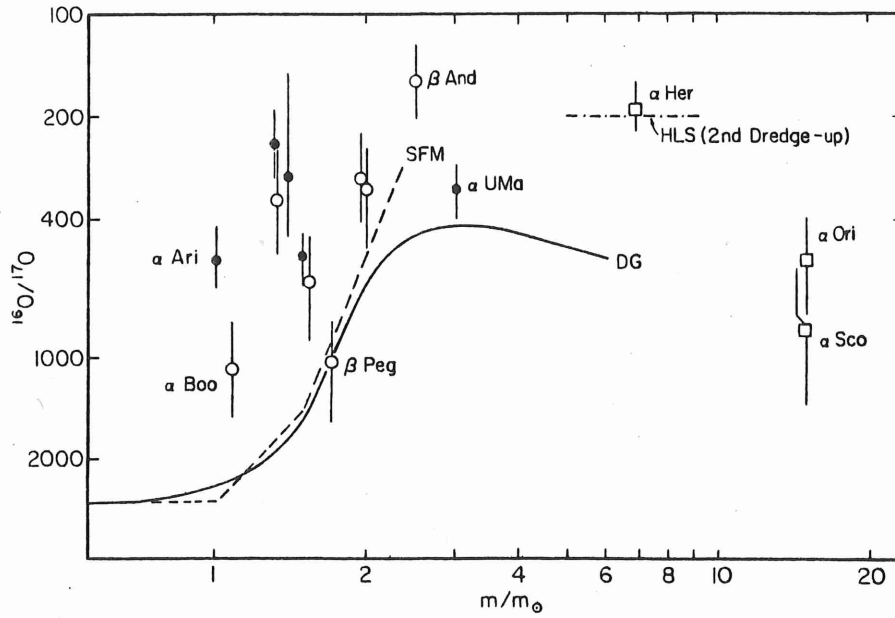
FIG. 4.—Predicted and observed $^{16}O/^{17}O$ ratios as a function of stellar mass. First dredge-up predictions are labeled *SFM* (*dashed line;* Shadick, Falk, and Mitalas 1980) and *DG* (*solid line;* Dearborn and Gough 1984). The second dredge-up prediction by HLS is shown by the dot-dash line. Ratios measured in this paper are represented by filled circles. Results from HL1 and HL2 are represented by the open symbols (*circles:* giants; *squares:* supergiants). Selected stars are identified by name.
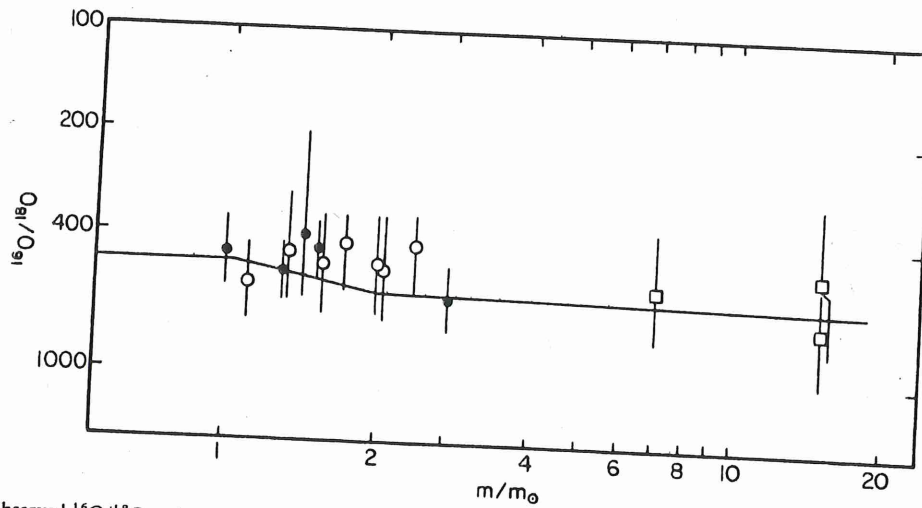

FIG. 5.—Predicted and observed $^{16}O/^{18}O$ ratios as a function of stellar mass. Full line shows the first dredge-up predictions by HL1 and HL2 using the "low" rate for $^{18}O(p, \alpha)^{15}N$ of Harris *et al.* (1983). *Open circles and squares:* ratios measured by HL1 and HL2. *Filled circles:* points measured in this paper.

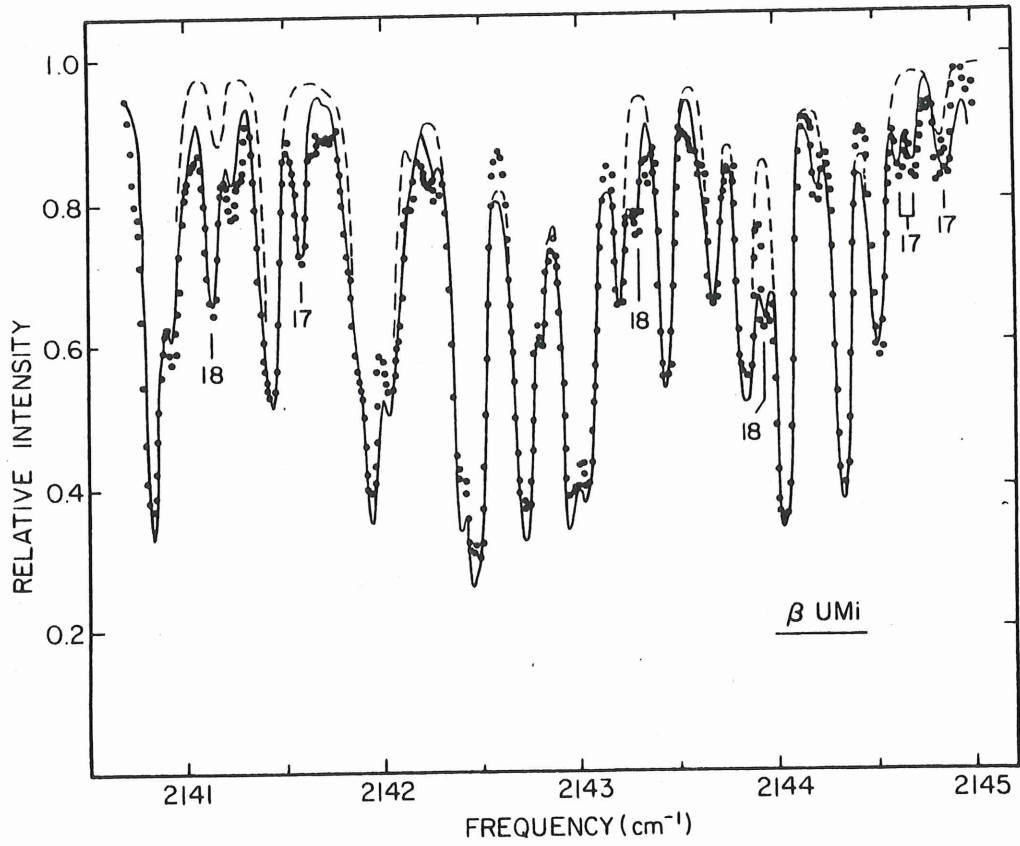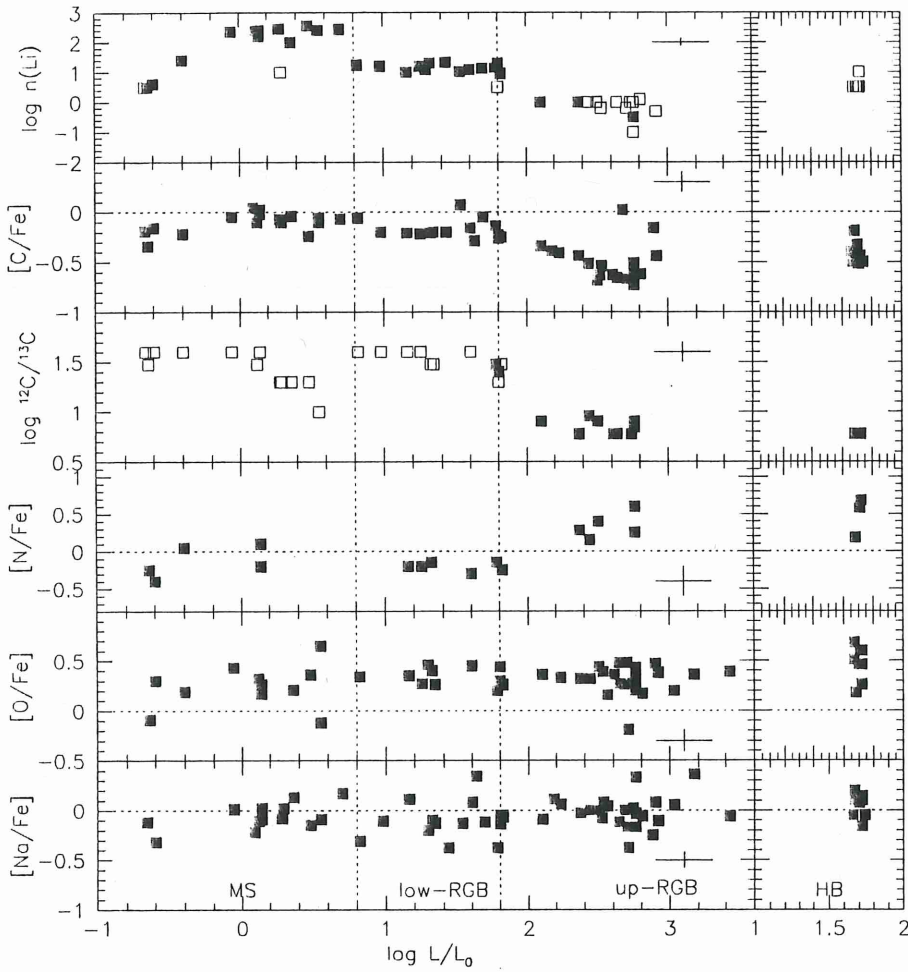Fig. 1.—Comparison of observed and synthesized spectra of β UMi. Synthetic spectra are shown for ${}^{16}O/{}^{17}O = {}^{16}O/{}^{18}O = 0$ (*dashed line*) and ${}^{16}O/{}^{17}O = 510$ and ${}^{16}O/{}^{18}O = 440$ (*solid line*). Principal contributors to some of the weaker lines are identified: $17 \equiv {}^{12}C{}^{17}O$ and $18 \equiv {}^{12}C{}^{18}O$.

Fig.
the a
and
$^{12}C/$
-2 ‹
tual i
lowe:
for tl
lines
(MS
RGB
ted s‹

Table 7. Average abundances in different evolutionary phases for stars with $-2 <$[Fe/H]< -1

Element		MS and TO			lower-RGB			upper-RGB	
$\log \epsilon(Li)$	12	2.40 ± 0.04	0.10	13	1.15 ± 0.03	0.12		< 0.0	
[C/Fe]	15	-0.09 ± 0.02	0.08	14	-0.14 ± 0.03	0.11	15	-0.58 ± 0.03	0.12
[N/Fe]	4	-0.11 ± 0.12	0.23	6	-0.21 ± 0.02	0.06	8	$+0.39 \pm 0.07$	0.21
[O/Fe]				16	$+0.34 \pm 0.03$	0.12	21	$+0.34 \pm 0.02$	0.09
[Na/H]				25	-0.09 ± 0.03	0.15	22	-0.02 ± 0.03	0.15
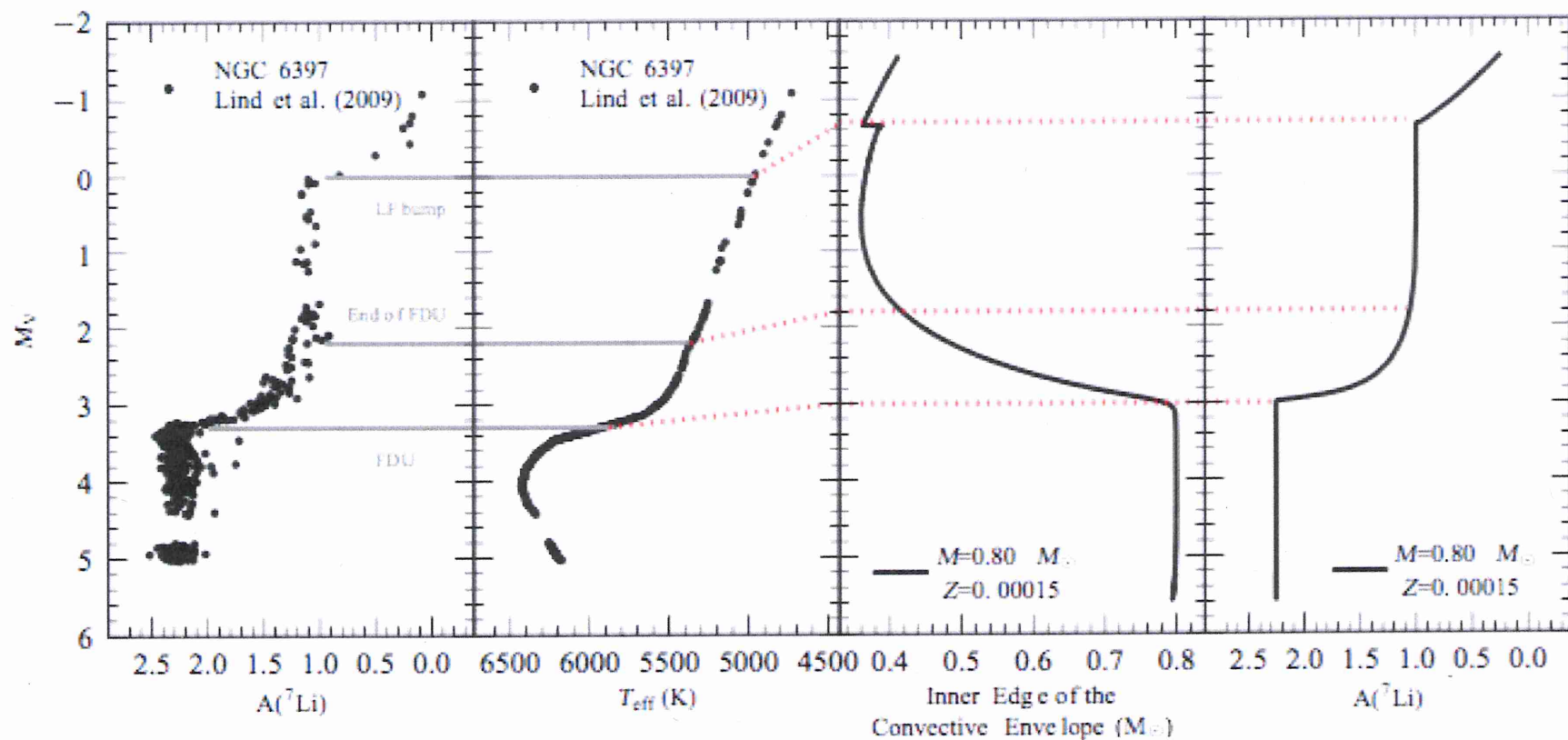
Figure 9. Observed behaviour of Li in stars in NGC 6397, from Lind et al. (2009), and as modelled by Angelou et al. (in preparation). The leftmost panel shows A(Li) = $\log_{10}$(Li/H) +12 plotted against luminosity for NGC 6397. Moving to the right the next panel shows the HR diagram for the same stars. The next panel to the right shows the inner edge of the convective envelope in a model of a typical red-giant star in NGC 6397. The rightmost panel shows the resulting predictions for A(Li) using thermohaline mixing and C = 120 (see Section 2.3.4). Grey lines identify the positions on the RGB where the major mixing events take place. Dotted red lines identify these with the theoretical predictions in the rightmost panels.
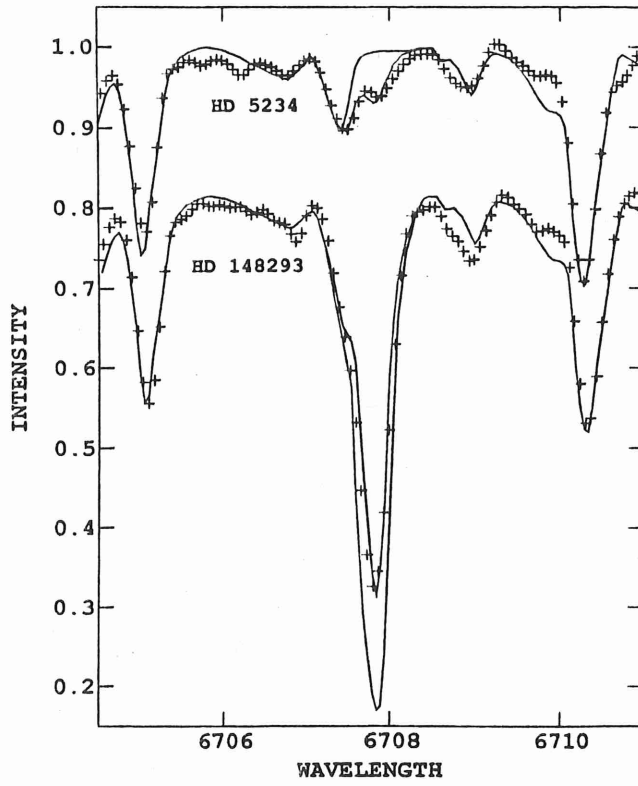
FIG. 4.—Observed and synthetic spectra for two stars. The plus signs are the observed spectra (after complete reduction). For the synthetic spectra (solid lines in the figure) we used model atmosphere parameters from Table 1 and Li abundances of $\log \varepsilon(Li) = +0.4$ and -8.0 for HD 5234, and $\log \varepsilon(Li) = +2.6$ and $+2.0$ for HD 148293.

FIG. 13.—Histogram of Li abundances for the program stars. The bin size for the abundance groups is 0.2 dex. The nondetections dominate the statistics below $\log \varepsilon(Li) \approx +0.5$.

Figure 2. Stars from our (blue symbols) and Brown et al. (1989) (green symbols) survey are shown (panel (a)) along with evolutionary track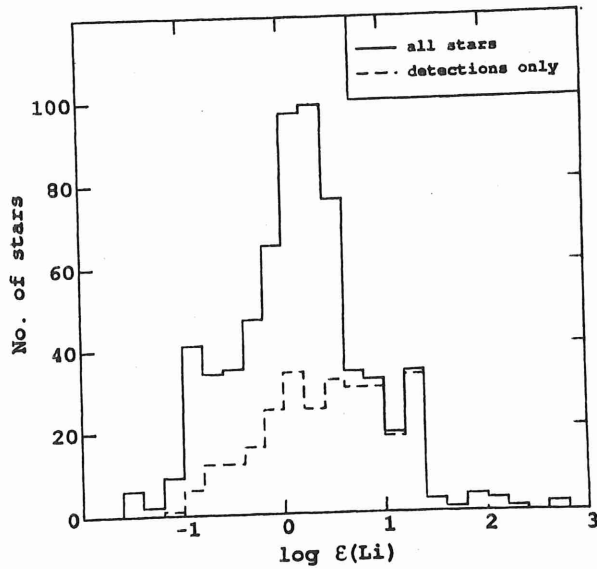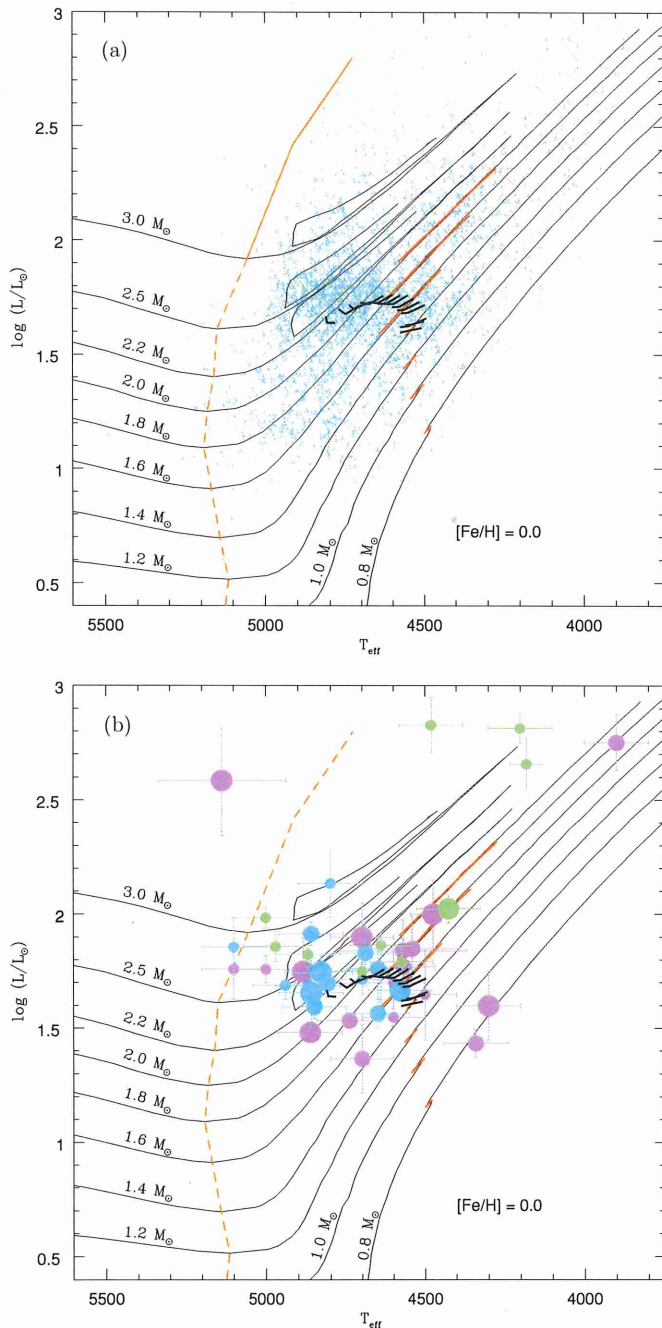s computed by Bertelli et al. (2008). Li-rich K giants are shown in panel (b): blue filled circles denote new Li-rich giants found in this study, green symbols are Li-rich giants from Brown et al. (1989), and magenta symbols are other Li-rich giants taken from the literature. Symbol size indicates amount of Li. The base of the RGB is shown as a broken red line and red portion on each of the tracks represents the location of the luminosity bump which is predicted to be seen for masses $M \leqslant 2\ M_\odot$. The thick black lines represent the clump region for He-core burning stars of masses 0.8–2.5 $M_\odot$.

(A color version of this figure is available in the online journal.)

masses up to 2 $M_\odot$ (Iben 1968; Bertelli et al. 2008) and a bump in the luminosity function along the RGB. As shown in Figure 2, the kink on the evolutionary tracks (Bertelli et al. 2008) is visible only up to 2 $M_\odot$ for solar metallicity stars.

Internally, the kink is associated with an inversion in the run of mean molecular weight with distance from the stellar center. This inversion is linked to destruction of ^{3}He by the

reaction ^{3}He(^{3}He, $2p$)^{4}He which lowers the mean molecular weight and the homogenization of the composition within the convective envelope. Eggleton et al. (2008) show that this inversion leads to "compulsory" mixing and changes to the surface abundances of C, N, and O isotopic abundances, i.e., the ^{12}C/^{13}C ratio is lowered relative to its value before the bump. Charbonnel & Lagarde (2010) recognize too that mixing occurs as a result of the molecular weight inversion but include the effects of rotationally induced mixing to drive the mixing. This mixing referred to as $\delta\mu$-mixing by Eggleton et al. (2008) or thermohaline mixing by Charbonnel & Lagarde (2010) is observationally confirmed by measurements of the ^{12}C/^{13}C ratio in giants along the RGB showing a decrease in the ratio at and above the luminosity of the bump.

As p-captures on ^{12}C create ^{13}C, the reservoir of primordial and main-sequence synthesized ^{3}He is depleted. It is this reservoir that is a potential source of ^{7}Li from the Cameron–Fowler (Cameron & Fowler 1971) mechanism (^{3}He(^{4}He, γ)^{7}Be(e^-, ν)^{7}Li) but in order for the ^{7}Li to enrich the stellar atmosphere it and its progenitor ^{7}Be must be swept quickly to temperatures too cool for proton captures to occur. Eggleton et al. (2008) calculations show that more than about 80% of the ^{3}He is destroyed in stars of masses less than about 1.5 $M_\odot$. This destruction seems unlikely to produce lithium because the mixing is too slow for the ^{7}Be and ^{7}Li to avoid destruction by protons (Lattanzio et al. 2008). However, the initial subsurface ^{3}He reservoir is such that only a minor fraction of the ^{3}He need to be converted with moderate efficiency to provide an Li-rich giant. It is anticipated that the lithium produced as the star crosses the bump's luminosity may be destroyed as the star with its convective envelope evolves to the tip of the RGB.

The evidence from Figure 2 is that few of the Li-rich stars are aligned along the run of bump stars in the H-R diagram. Although the cooler Li-rich stars are likely to be bump stars, many Li-rich stars are too warm to be so identified. Thus, we suggest that Li-rich stars cannot be identified exclusively with the bump. Rather the co-location of the Li-rich stars in Figure 2 with the high concentration of observed (Li-normal) giants and the theoretical location of the clump suggest that they are clump stars. If Li produced at the bump on the RGB survives a star's evolution from the bump to the clump, such Li-rich stars from the survey may nonetheless appear predominantly as clump stars because the lifetime at the clump is similar to or longer than the time to evolve through the bump and to the clump via the tip of the RGB. Since Li, if produced at the bump on the RGB, may be destroyed by the time the star has evolved up the RGB to experience the He-core flash, the speculation is that the Cameron–Fowler mechanism may also operate at the He-core flash in at least some stars, i.e., in stars of $M < 2.25\ M_\odot$. Since Eggleton et al. (2008) predict survival of ^{3}He in stars with $M > 1.5\ M_\odot$, there seems in principal the possibility that the He-core flash may be the key to synthesis of lithium in stars in a narrow mass range centered at about 2 $M_\odot$ with the range's the upper limit set by the maximum mass for a He-core flash and the lower limit set by survival of sufficient ^{3}He following $\delta\mu$ or thermohaline mixing on the RGB. Evidently, the concentration of Li-rich stars at the clump implies that the synthesized Li is swiftly destroyed as a clump star evolves along the early reaches of the AGB. If all stars evolving through the He-core flash synthesize copious amounts of Li, they survive as an Li-rich giant for about 1% of their horizontal branch lifetime, i.e., about 2 Myr. (The four luminous Li-rich stars in Figure 2
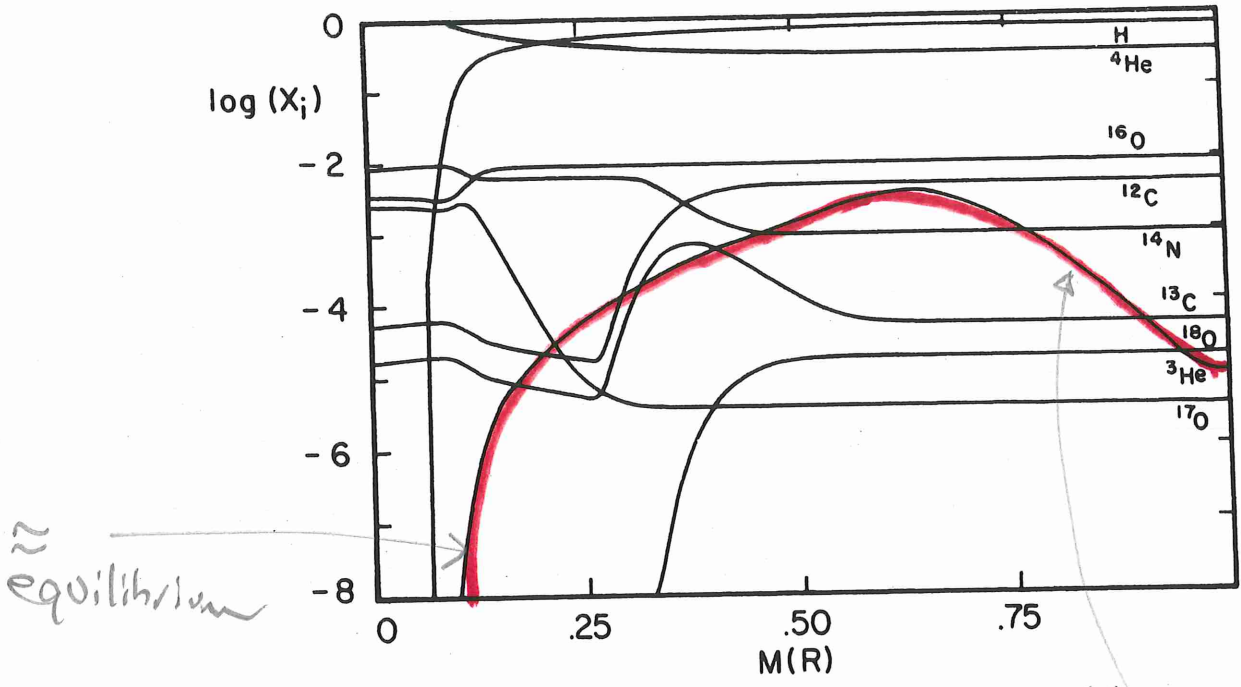
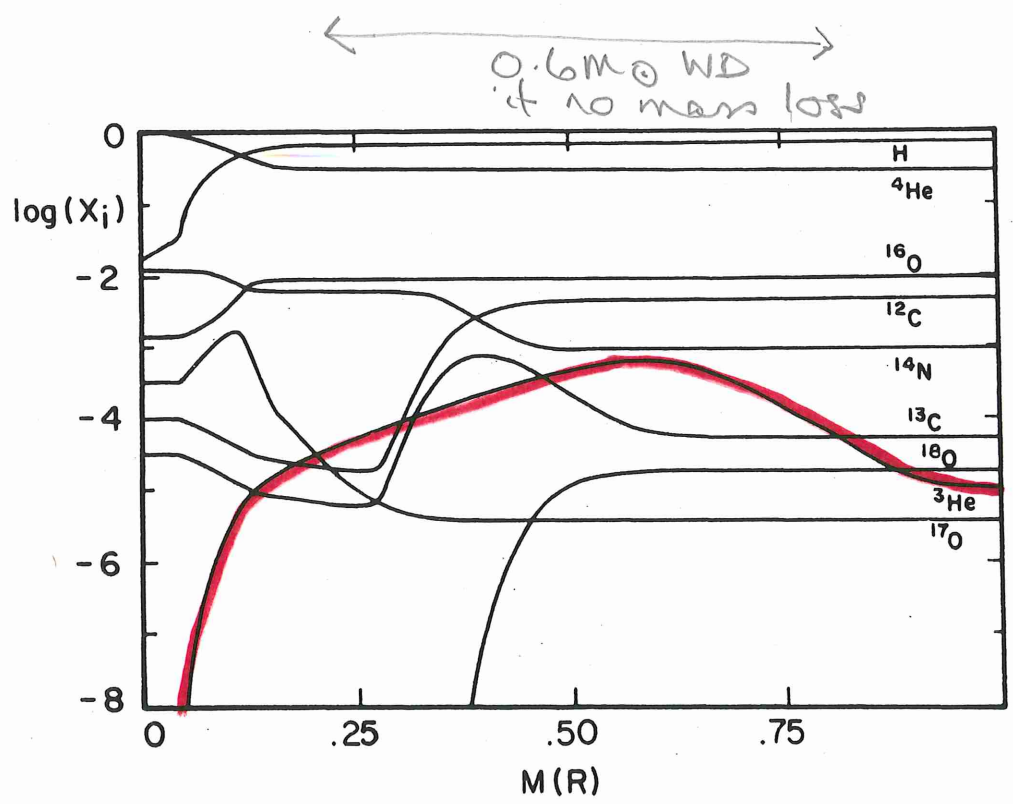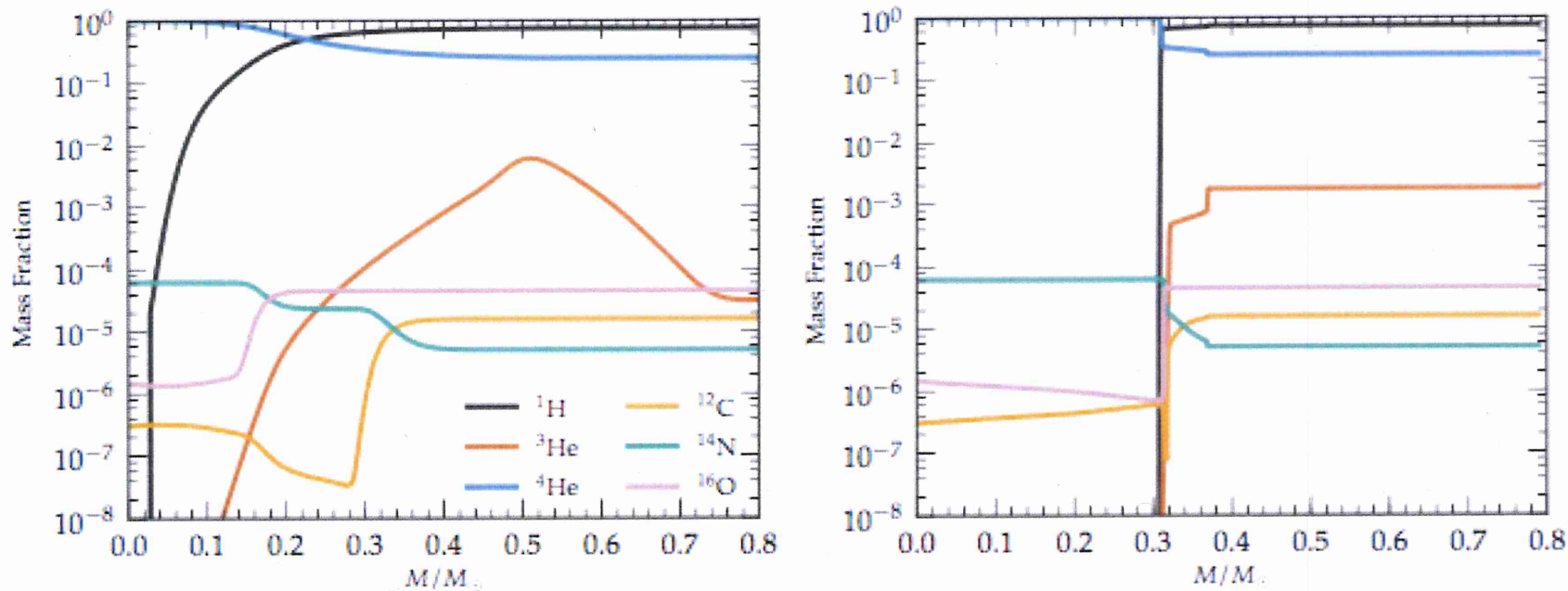FIG. 1.—Composition of a 1 $M_\odot$ star near the end of its main-sequence evolution

equilibrium

0.6 $M_\odot$ WD
if no mass loss

NOT in
equilibrium

FIG. 2.—Composition of a 2 $M_\odot$ star near the end of its main-sequence evolution

0.6 $M_\odot$ WD

Figure 12. Abundance profiles in a 0.8 M$_\odot$ model with Z = 0.00015 (see also Figure 9). The left panel shows a time just after core hydrogen exhaustion and the right panel shows the situation soon after the maximum inward penetration of the convective envelope. At this time the hydrogen burning shell is at $m(r) \approx 0.31$ M$_\odot$ and the convective envelope has homogenised all abundances beyond $m(r) \approx 0.36$ M$_\odot$. The initial ^{3}He profile has been homogenised throughout the mixed region, resulting in an increase in the surface value, which is then returned to the interstellar medium through winds, unless some extra-mixing process can destroy it first.

THIRD DREDGE-UP at AGB TTP

- ## STRUCTURE

  - H-BURNING SHELL → MASS OF He SHELL CONVECTIVE ENVELOPE SEP. FROM

    H-BURNING SHELL

  - He SHELL MASS INCREASE → He SHELL IGNITION → CONVECTION FOR BRIEF WHILE (≡ THERMAL PULSE)

  - H BURNING SHELL → EXTINGUISHED

  - CONVECTIVE ENVELOPE DESCENDS INTO TOP OF FORMER H BURNING SHELL AND TO TOP OF FORMER He BURNING PULSE

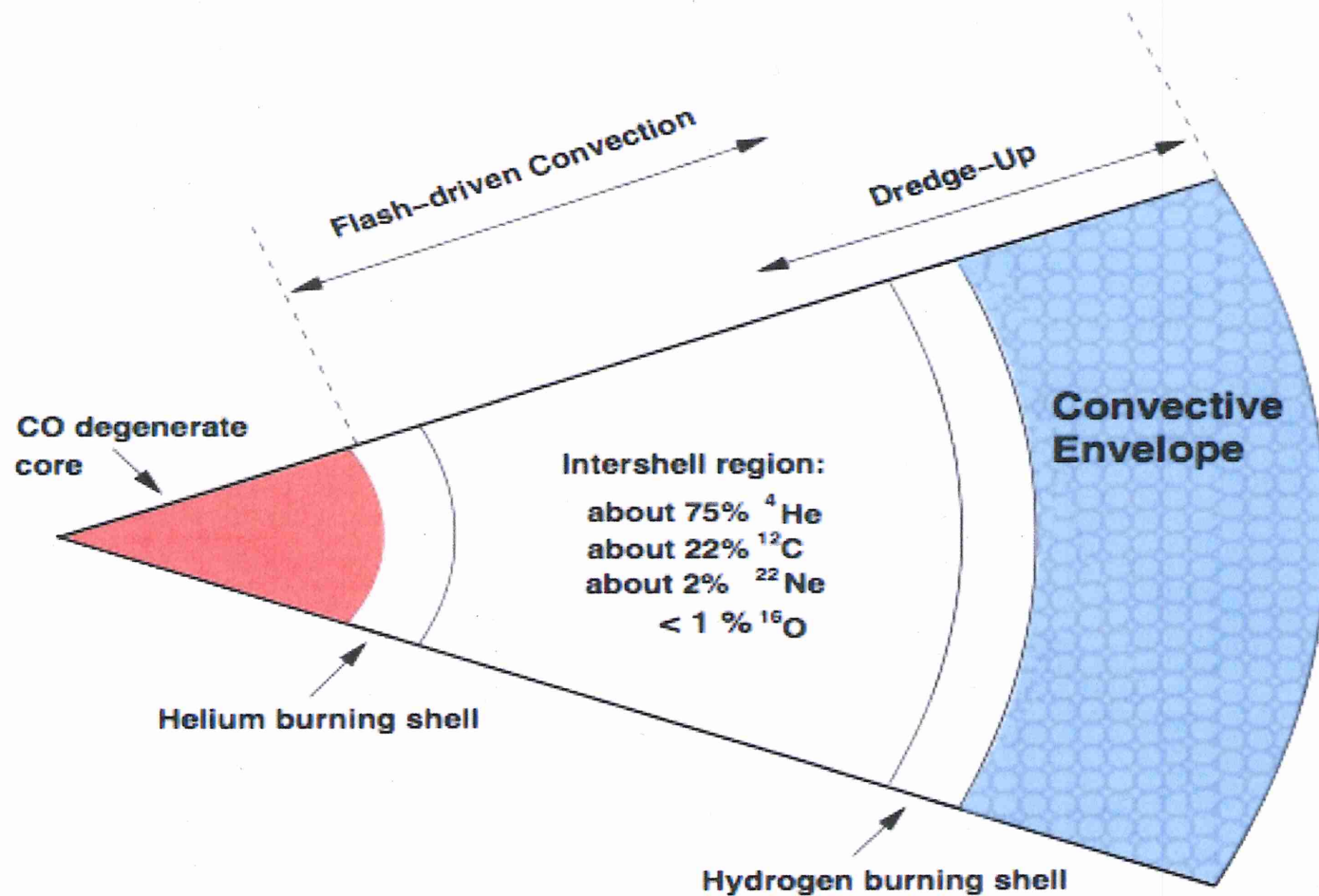   ## He and H-BURNING PRODUCTS → ENVELOPE ≡ ATMOSPHERE

    C-O CORE HAS GROWN

    H-BURNING SHELL RESUMES

Figure 14. Schematic structure of an AGB star showing the electron-degenerate core surrounded by a helium-burning shell above the core, and a hydrogen-burning shell below the deep convective envelope. The burning shells are separated by an intershell region rich in helium (~75%) and carbon (~22%), with some oxygen and ^{22}Ne. A super-AGB star has an O–Ne degenerate core otherwise the qualitative schematic structure remains the same. From Karakas, Lattanzio, & Pols (2002). Click on the image to run an animation of a pulse cycle.
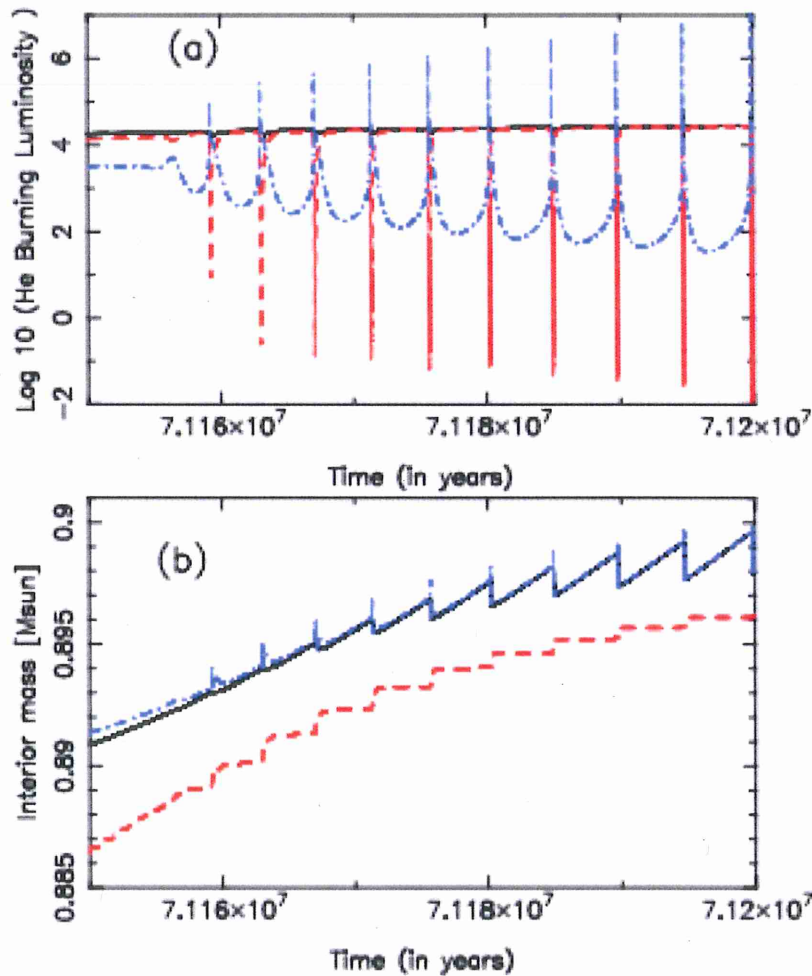
Figure 15. Evolution of the luminosities and core masses (in solar units) for a 6 M$_\odot$, $Z = 0.02$ model during the start of the TP-AGB. Each panel shows the evolution during the first 10 thermal pulses. Panel (a) shows the surface (or radiated) luminosity (black solid line), H-burning shell luminosity (blue dot-dashed line), and He-burning shell luminosity (red dashed line). Panel (b) shows the masses of the H-exhausted core (black solid line), He-exhausted core (red dashed line), and the inner edge of the convective envelope (blue dot-dashed line).

DREDGE-UP SEEN IN 'ALL CALCS.
after sufficient number of pulses

- $\dot{m}$ · IMPORTANT BUT UNCERTAIN
  (OBS. + THEORY)
  - · INCREASES WITH LUMINOSITY (?)

  - · REDUCES m(ENVELOPE) → STOPS
    NUCLEAR BURNING

- S-process [Tc et al.]

  - · NEUTRON SOURCE & ITS SITE u(OV)
    - · OLD IDEA

    - · NEW IDEA

  - · ^{13}C POCKET
    - · DIFFUSION OF p INTO
      He-SHELL $^{12}C(p,\gamma)^{13}C$ 'only'
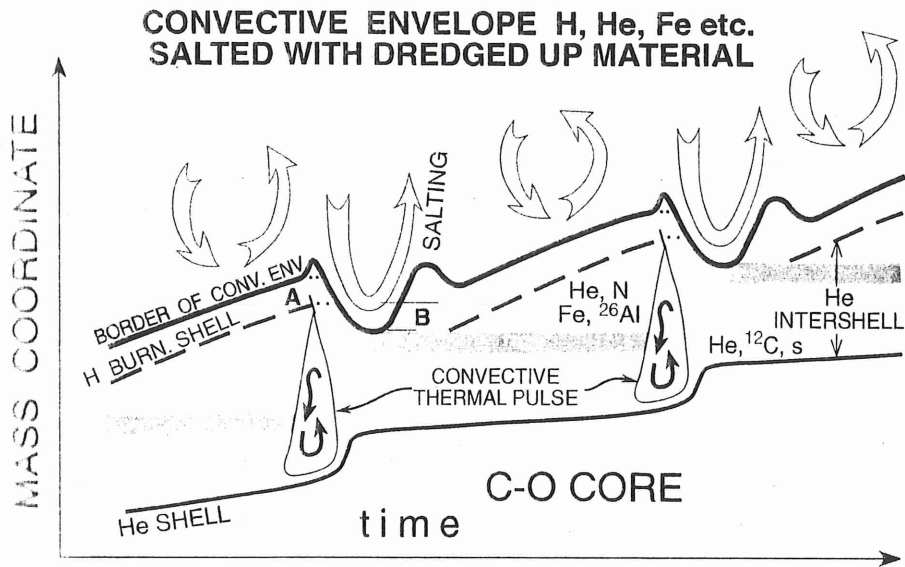   BUT HOW MUCH?

Figure 5 Illustration of the structure of a thermal pulse-asymptotic giant branch star over time, showing the border of the convective envelope, the H-burning shell, and the He-burning shell. The region between the H and He shells is the He intershell. *Horizontal gray bars* represent zones where protons are assumed to be ingested to make ^{13}C. In the earlier models, ^{13}C was not allowed to burn until the region was engulfed in a convective pulse. In the newer models, ^{13}C is naturally burned under radiative conditions in the gray area before ingestion because of the progressive heating of the region. The slow neutron capture products are then engulfed by the thermal pulse, and further processing occurs owing to neutrons from the ^{22}Ne$(\alpha,n)^{25}$Mg source. Region A between the H shell and the border of the convective zone and region B in the He intershell are mixed into the convective envelope during TDU, and these regions salt the envelope with freshly synthesized material. The remaining part of the He intershell region below B is also enriched in s-process nuclides and is partly mixed over subsequent cycles. Note that the convective thermal pulse does not reach the H-burning shell, as found by Iben (1977).

TP-AGB n-s FACTORS

- EFFICIENCY OF TDU
- MIN. CORE MASS FOR TDU
  TO BEGIN
  $\rightarrow$ N(TP) before $\eta\dot{m}$ KILLS TP
- SIZE OF CONVECTIVE ENVELOPE
- MASS OF He INTERSHELL